Role of the deformation potential in ultrasonic attenuation by open-orbit electrons in copper

W. M. Theis* and J. D. Gavenda
Department of Physics, University of Texas at Austin, Austin, Texas 78712
(Received 24 October 1978)

We have carried out a model calculation of ultrasonic attenuation in copper as a function of applied magnetic field for shear waves propagating along [111] and $\vec{B}$ along [11$\bar{2}$] so as to give open-orbit resonances. The results are in qualitative agreement with our measurements if we use a deformation potential based on the strained-energy-band calculations of Gray and Gray. Better agreement is obtained by fitting a model-deformation-potential function of proper symmetry to certain features of the experimental data. However, we are unable to reproduce the dip in attenuation at the fundamental resonance which is observed experimentally for sound polarization along $\vec{B}$. The discrepancy may be caused by one of the assumptions made to simplify the calculations, which include using the free-electron approximation for all but those electrons on open orbits, taking the electron mean-free path along $\vec{q}$ to be constant, and assuming that the ionic current is perfectly screened by the electrons.

I. INTRODUCTION

Although some 20 years have elapsed since the magnetoacoustic effect was first discovered, its full potential as a tool for measuring conduction-electron peoperties has not been realized. The major stumbling block has been the absence of a straightforward method for relating the experimental data to those electronic properties.

There have been two widely disparate theoretical approaches to magnetoacoustic calculations. First, a purely free-electron or jellium treatment in which the only forces acting on the electrons are those caused by collision drag and the self-consistent electric field. This approach is exemplified in papers by Rodriguez,[1] Kjeldaas,[2] and Cohen, Harrison, and Harrison.[3] Second, there is a real-metal treatment in which the calculations are carried out in a reference frame moving with the ions. There is a deformation force related to the shift in electron energy caused by lattice strain. There is no collision-drag force in this frame, but fictitious forces arise from the acceleration of the reference frame. A self-consistent electric field also acts to keep the net current near zero. Pippard[4] and various other authors[5] have set up the theoretical framework for this approach.

The deformation theories require knowledge of the deformation potential over the Fermi surface, but very little is known about deformation potentials in metals. As a consequence there have been a number of attempts to use the jellium theory to explain magnetoacoustic phenomena in real metals. Satisfactory results have been obtained for metals with essentially spherical Fermi surfaces, but major discrepancies arise for metals with Fermi-surface shapes which lead to sharp resonances in the ultrasonic attenuation, especially when shear waves are considered as in the following examples.

Doppler-shifted cyclotron resonance for $\vec{q} \parallel \vec{B}$, where $\vec{q}$ is the sound propagation vector and $\vec{B}$ the applied magnetic field, is found to cause pronounced peaks in attenutation at values of B for which an entire band of electrons is simultaneously in resonance with the sound field.[6] However, the jellium theory predicts dips, or antiresonances.[7]

Resonant attenuation of shear waves by open-orbit electrons drifting along $\vec{q}$ also leads to pronounced peaks[8] (with an important exception to be discussed below). The jellium model again predicts dips, or antiresonances.[9]

Various authors[10] have managed to get peaks rather than dips for the cases just described by using the deformation theory while ignoring the self-consistent electric field force which would greatly complicate the calculations. Neither they nor anyone else, however, have succeeded in getting quantitative agreement between calculated and measured attenuation data.

In 1973 Khatri and Peverley[11] (KP) found the first clear example of a dip or antiresonance in experimental data. In a copper crystal with $\vec{q} \parallel [111]$ and $\vec{B} \parallel [11\bar{2}]$ so as to produce open orbits along $\vec{q}$, they found that resonant attenuation of shear waves resulted in either peaks or dips, depending on the direction of the polarization vector. It is obvious that a correct theoretical treatment must explain both dips and peaks in the same metal under virtually identical experimental conditions. We therefore chose this geometry for a model calculation which includes both deformation and self-consistent electric field forces.

Before undertaking the calculation we repeated

the KP experiment over a wider range of magnetic fields and took great pains to eliminate experimental errors. Our methods and the resulting data are presented in Sec. II. The equations we used in the model calculation are derived in Sec. III. In Sec. IV we describe how electron energy shifts calculated by Gray and Gray[12] (GG) for certain points on the copper Fermi surface were fitted to an interpolation function to give the deformation potential. The attenuation calculated for this deformation potential is compared with the experimental curves and then, in Sec. V, we show a model deformation potential which gives a somewhat better fit to experiment. In Sec. VI we summarize our results and speculate why the model calculations fail to give dips as pronounced as those found experimentally.

II. EXPERIMENTAL METHODS AND RESULTS

A. Specimen

Open-orbit resonances are observed when the trajectory of the orbit is parallel to $\vec{q}$ and $D=n\lambda$, where $D=\hbar K/eB$ is the period of the open orbit in real space, K is the period in $\vec{k}$ space, $e=1.6\times10^{-20}$ emu, λ is the sound wavelength, and n is an integer. Obviously the electron mean free path l must be greater than D in order for resonances to occur, thus one requires $ql\gg1$.

We used a specimen cut from a single-crystal copper boule[13] with a residual-resistance ratio of 35 000. Faces perpendicular to [111] were spark planned and etched before 30- or 50-MHz AC-cut quartz transducers were attached with Nonaq stopcock grease. The thickness of the specimen was 2.87 mm. Even at 30 MHz this specimen had $ql\gg1$.

B. Alignment of the magnetic field

In order to obtain reproducible line shapes for the resonances we found it necessary to have $\vec{B}\perp\vec{q}$ to better than 0.1°. We discovered that our 15-in. electromagnet did not rotate about an axis precisely perpendicular to $\vec{B}$; therefore we shimmed the magnet on its rotating mount until the discrepancy, measured by reflecting a laser beam from the pole faces, was less than 0.1°.

Each experimental run began with a polar plot of the attenuation at fixed B. The specimen holder was tilted about two perpendicular axes, using micrometer adjustments, until the polar plot showed the proper symmetry for the geometry of the experiment. Errors of less than 0.1° are easily detected from such polar plots.[14]

C. Electronic apparatus

Since we wanted to compare measured line shapes with calculations based on constant q or λ, we employed a phase-locked oscillator frequency control which maintained constant λ in spite of variations in the velocity of sound near resonances. The electronic apparatus, shown in Fig. 1, is similar to that described elsewhere[15] except that the electrical feed-through problem has been eliminated by using a gated oscillator rather than continuous waves. Also, an analog divider in the frequency control loop divides out signal amplitude variations over a 40-dB range, thus increasing the dynamic range over which the phase remains locked. The system operates in the following manner: The signal from the specimen is split by a power divider and mixed in balanced detectors with the in-phase and quadrature reference signals. If the signal at the transmitting transducer is $E_0\cos\omega t$, at the receiving transducer it will be $E_0e^{-2\alpha L}e^{iqL}\cos\omega t$ after traveling a distance L through the sample. The dc output of the in-phase mixer is

$$E_\alpha=E_0e^{-2\alpha L}\cos qL,$$

while that of the quadrature mixer is

$$E_q=E_0e^{-2\alpha L}\sin qL.$$

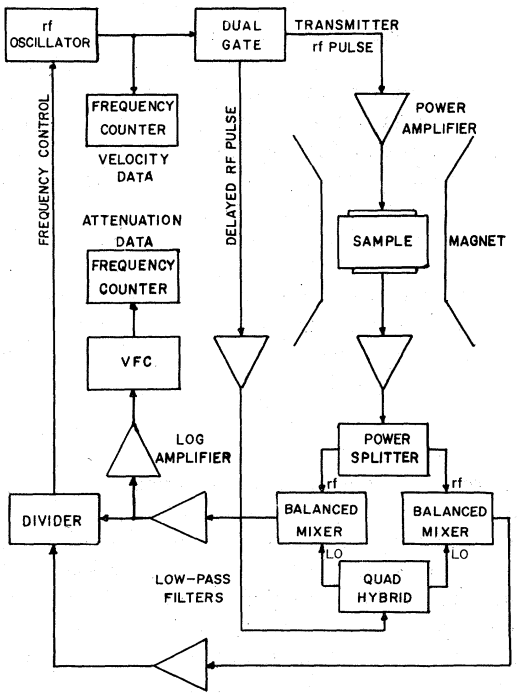

FIG. 1. Block diagram of the electronic apparatus. VFC designates a voltage-to-frequency converter.

Since $q=\omega/v_s$, the frequency can be adjusted to a value ω_0 (say at $B=0$) such that $\cos q_0 L=1$, i.e., $q_0=2\pi n/L$, where n is the number of sound wavelengths in the sample. Note that this condition causes the quadrature output to be zero.

Application of a magnetic field will cause the zero-field sound velocity v_s^0 to change to $v_s^0+\Delta v_s$, so that $qL\neq 2\pi n$. The quadrature output voltage E_q will cause the oscillator frequency to change by

$$\Delta\omega=-KGE_q,$$

where G is the feedback-loop gain and K is the frequency/V coefficient for the oscillator frequency control. When the system reaches equilibrium,

$$q=(\omega_0+\Delta\omega)/(v_s^0+\Delta v_s).$$

For $\Delta v_s\ll v_s^0$ and $\Delta\omega\ll\omega_0$,

$$E_q\approx E_0 e^{-2\alpha L} q_0 L(\Delta\omega/\omega_0-\Delta v_s/v_s^0).$$

To make the feedback-loop gain independent of the signal amplitude, an analog divider is included to divide E_q by E_α before it goes to the frequency control so that

$$\Delta\omega=-KGq_0 L(\Delta\omega/\omega_0-\Delta v_s/v_s^0).$$

We can now solve for $\Delta\omega$ in terms of Δv_s:

$$\frac{\Delta\omega}{\omega_0}=\frac{\Delta v_s}{v_s^0}\frac{1}{1+\omega_0/KGq_0L}.$$

For $KGq_0L\gg\omega_0$, $\Delta\omega/\omega_0=\Delta v_s/v_s^0$, thus the frequency shift will accurately represent the relative velocity if the gain G is made as large as possible. The characteristics of the active filter in the feedback loop were chosen to minimize instabilities, so the system remains phase locked and linear (to within 5%) over a 40-dB dynamic range. The frequency counter on the oscillator yields velocity shifts with a precision of about 10^{-5}.

The attenuation signal is coupled to a voltage-to-frequency converter and counter to produce a digital output. The frequency counter on the gated oscillator provides a digital representation of the velocity. These digital values are punched on paper tape for successive values of B established by a digital magnetic field control unit.

D. Experimental results

Figure 2 displays attenuation versus D/λ for polarization of sound parallel and perpendicular to $\vec{B}$. Note that a large peak in attenuation occurs for ion velocity $\vec{u}\parallel\vec{B}$ at $D/\lambda=1$, while a small dip occurs for $\vec{u}\perp\vec{B}$. The depth of the dip is proportional to frequency in the 25–40-MHz range. At $D/\lambda=2$ the situation is reversed. The higher resonances for $\vec{u}\parallel\vec{B}$ have complex structures, so we confine our attention to the first two resonances in the sections which follow.

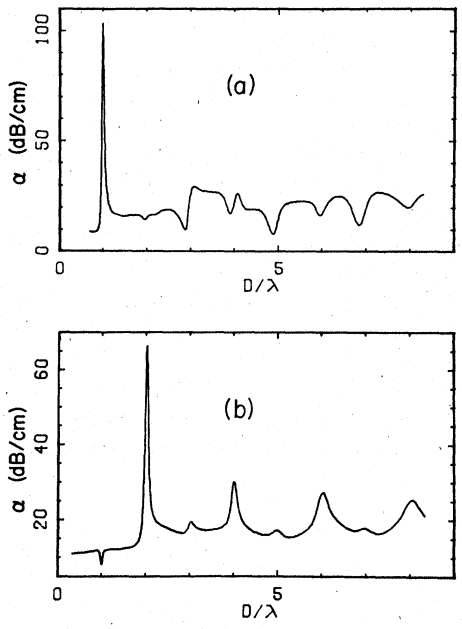

FIG. 2. Measured attentuation of shear waves propagating along [111] in copper with $\vec{B}\parallel[11\bar{2}]$. D is the period of the open orbit and is inversely proportional to B. (a) Polarization parallel to $\vec{B}$ at a frequency of 46.9 MHz. (b) Polarization perpendicular to $\vec{B}$ at a frequency of 35.7 MHz.

III. CALCULATION OF ATTENUATION FOR OPEN ORBITS

The method adopted for the calculation of ultrasonic attenuation in the presence of a magnetic field is based on Pippard's theory.[4] The forces on the electrons are taken to be those arising from the deformation potential and a self-consistent electric field, viewed from a reference frame moving with the crystal lattice. A relaxation time τ is assumed to describe the scattering of the electrons back to equilibrium. The sound frequency and magnetic field strength are assumed small enough to allow the electrons to screen the ionic current completely.

We choose coordinates such that $\vec{B}$ is along z and $\vec{q}$ is along x. Although the acoustic and electromagnetic fields vary as $e^{i(qx-\omega t)}$, the equations are greatly simplified if we ignore the time dependence. The approximation is valid for $\omega\tau\ll 1$, where ω is the sound frequency.

If a force $\vec{\Pi}e^{iqx}$ acts on the electrons, the excess energy of those which arrive at $x=0$ when $t=t_0$ is

$$\Delta\epsilon=\int_{-\infty}^{t_0}\vec{\Pi}\cdot\vec{v}e^{iqx}\exp\left(-\int_t^{t_0}\frac{dt'}{\tau}\right)dt. \qquad (1)$$

This can be transformed to an integration over k_y by using the equation of motion, $dk_y=(K/D)v_x\,dt$, where $K/D=eB/\hbar$. Since $x=(D/K)(k_y-k_y^0)$, where

$k_y^0 = k_y(t_0)$,

$$\Delta\epsilon = \left(\frac{D}{K}\right)\int_{k_y^{-\infty}}^{k_y^0}\left(\frac{\vec{\Pi}\cdot\vec{\nabla}}{v_x}\right)\exp\left[iq\left(\frac{D}{K}\right)(k_y - k_y^0)\right]$$

$$\times\exp\left[-\left(\frac{D}{K}\right)\int_{k_y}^{k_y^0}(v_x\tau)^{-1}dk_y'\right]dk_y, \qquad (2)$$

where $k_y^{-\infty} = k_y(t\to-\infty)$.

When dealing with open orbits along $\vec{q}$, i.e., along k_y, this integral can be reduced to a sum by making use of the periodic properties of $\vec{\Pi}(k_y)$ and $\vec{\nabla}(k_y)$. We expand

$$\frac{\vec{\Pi}\cdot\vec{\nabla}}{v_x} = \sum_{n=-\infty}^{\infty} a_n \exp\left(\frac{-2\pi i n k_y}{K}\right), \qquad (3)$$

where

$$a_n(k_z) = K^{-1}\int_{-K/2}^{K/2}\left(\frac{\vec{\Pi}\cdot\vec{\nabla}}{v_x}\right)\exp\left(\frac{2\pi i n k_y}{K}\right)dk_y. \qquad (4)$$

Note that there are generally two sets of $a_n(k_z)$, corresponding to $k_x>0$ and $k_x<0$, respectively.

As a further simplification we assume that the relaxation time is such that $l_x = v_x\tau$ is constant. With these definitions and assumptions Eq. (2) reduces to

$$\Delta\epsilon(\vec{k}) = l_x\sum\frac{a_n(k_z)\exp(-2\pi i n k_y/K)}{1+iql_x(1-n\lambda/D)}. \qquad (5)$$

The electronic current can now be calculated from

$$\vec{J} = \left(-\frac{e}{4\pi^3\hbar}\right)\int\left(\frac{\vec{\nabla}}{v}\right)\Delta\epsilon\, dS. \qquad (6)$$

One can show that $dS/v = dk_y\, dk_z/v_x$ on the Fermi surface, so Eq. (5) substituted into Eq. (6) yields

$$\vec{J} = -\frac{el_x}{4\pi^3\hbar}\sum\frac{\int a_n\, dk_z}{1+iql_x(1-n\lambda/D)}$$

$$\times\int\left(\frac{\vec{\nabla}}{v_x}\right)\exp\left(-\frac{2\pi i n k_y}{K}\right)dk_y. \qquad (7)$$

Replacement of $\vec{\Pi}\cdot\vec{\nabla}$ by $\vec{\nabla}$ in Eq. (4) causes the second integral to become $K\vec{\nabla}_n^*(k_z)$, so

$$\vec{J} = -\frac{el_xK}{4\pi^3\hbar}\sum\frac{\int a_n\vec{\nabla}_n^*\,dk_z}{1+iql_x(1-n\lambda/D)}. \qquad (8)$$

We set $\vec{\Pi} = -e\vec{E}$ in Eq. (4), find the current $\vec{J}$ caused by $\vec{E}$, and define the conductivity $\underline{\sigma}$ by $\underline{\sigma}\cdot\vec{E} = \vec{J}$. The result is

$$\underline{\sigma} = \frac{e^2l_xK}{4\pi^3\hbar}\sum\frac{\int\vec{\nabla}_n^*\vec{\nabla}_n\,dk_z}{1+iql_x(1-n\lambda/D)}. \qquad (9)$$

In order to find the attenuation we must calculate the total excess energy $\Delta\epsilon_t$ resulting from the deformation force $\vec{\Pi}^{\rm def}$ and the self-consistent electric field force $-e\vec{E}^{\rm sc}$. The attenuation is given by

$$\alpha = (4\pi^3\hbar Mv_su^2)^{-1}\int\left(\frac{|\Delta\epsilon_t|^2}{l}\right)dS, \qquad (10)$$

where M is the density of the metal, v_s the velocity of sound, and u the particle velocity.

The assumption of perfect screening implies that

TABLE I. Deformation-potential interpolation functions and coefficients fitted to values calculated by Gray and Gray. The summation $\sum$ implies a permutation of the crystal coordinates $\hat{k}_1$, $\hat{k}_2$, and $\hat{k}_3$. Here, $C(\frac{1}{2}x)\equiv\cos(\frac{1}{2}k_1a_0)$, $S(\frac{1}{2}x)\equiv\sin(\frac{1}{2}k_1a_0)$, etc.

Case	Fitted coefficient (Ry)	Function
Hydrostatic	0.393	$\sum C(\frac{1}{2}x)C(\frac{1}{2}y)$
	−0.201	$\sum C(x)$
	−0.952	$\sum C(x)C(\frac{1}{2}y)C(\frac{1}{2}z)$
Tetragonal	−0.274	$2C(\frac{1}{2}x)C(\frac{1}{2}y) - C(\frac{1}{2}x)C(\frac{1}{2}z)$ $-C(\frac{1}{2}y)C(\frac{1}{2}z)$
	−0.110	$C(x)+C(y)-2C(z)$
	−0.062	$C(\frac{1}{2}z)[C(\frac{1}{2}x)C(y)+C(x)C(\frac{1}{2}y)]$ $-2C(z)C(\frac{1}{2}x)C(\frac{1}{2}y)$
Trigonal	−0.740	$\sum S(\frac{1}{2}x)S(\frac{1}{2}y)$
	−0.261	$\sum S(z)[S(\frac{1}{2}x)C(\frac{1}{2}y)+C(\frac{1}{2}x)S(\frac{1}{2}y)]$ $+\frac{1}{2}\sum C(z)S(\frac{1}{2}x)S(\frac{1}{2}y)]$
	−0.679	$\sum S(x)C(y)$

the current produced by $\vec{E}^{sc}$ must be the negative of $\vec{J}^{def}$, the current produced by $\vec{\Pi}^{def}$, therefore

$$\underline{\sigma}\vec{E}^{sc} = -\vec{J}^{def}. \tag{11}$$

If we take Eq. (8) to define $\vec{J}^{def}$ when a_n is a Fourier coefficient of $\vec{\Pi}^{def}\cdot\vec{v}/v_x$, we obtain

$$\vec{E}^{sc} = \frac{el_xK}{4\pi^3\hbar}\underline{\sigma} - 1\sum \frac{\int a_n\vec{v}_n^* dk_z}{1+iql_x(1-n\lambda/D)}. \tag{12}$$

Now, with $\vec{\Pi} = \vec{\Pi}^{def} - e\vec{E}^{sc}$ in Eq. (4), Eq. (5) yields

$$\Delta\epsilon_t = l_x\sum \frac{(a_n - e\vec{E}^{sc}\cdot\vec{v}_n)\exp(-2\pi i n k_y/K)}{1+iql_x(1-n\lambda/D)}, \tag{13}$$

and the attenuation is

$$\alpha = \frac{Kl_x}{4\pi^3\hbar M v_s u^2}\sum \frac{\int_i |a_n - e\vec{E}^{sc}\cdot\vec{v}_n|^2 dk_z}{1+q^2l_x^2(1-n\lambda/D)^2}. \tag{14}$$

The final result contains a term entirely due to the deformation potential, one due to the self-consistent field, and a term involving both. These can be written

$$\alpha = \alpha_{def} + \alpha_{sc} + \alpha_i, \tag{15}$$

where

$$\alpha_{def} = \sum A_n \int |a_n|^2 dk_z, \tag{16}$$

$$\alpha_{sc} = e^2\sum A_n \int |\vec{E}^{sc}\cdot\vec{v}_n|^2 dk_z, \tag{17}$$

$$\alpha_i = -2e\sum A_n \mathrm{Re}\left(\vec{E}^{sc}\cdot\int \vec{v}_n a_n^* dk_z\right), \tag{18}$$

and

$$A_n = \frac{Kl_x}{4\pi^3\hbar M v_s u^2}[1+q^2l_x^2(1-n\lambda/D)^2]^{-1}. \tag{19}$$

The first two contributions to the attenuation are clearly positive, but it is not so obvious what the sign of α_i will be. We next introduce a model deformation potential for a specific metal, copper, and evaluate the components of α.

IV. DEFORMATION-POTENTIAL INTERPOLATION FUNCTION

Gray and Gray[12] have computed electron energy shifts at four high-symmetry points on the copper Fermi surface for hydrostatic, tetragonal, and trigonal strains. The relationship between these shifts and Pippard's deformation force will now be explored.

In the reference frame moving with the ions, the effect of a sudden strain $\underline{\epsilon}$ is to change the wave vector of an electron on the Fermi surface by an amount $\Delta\vec{k} = -\underline{\epsilon}\cdot\vec{k}$. The electron tends to relax back to the new equilibrium Fermi surface, which has shifted by an amount $\Delta\vec{k}_F$ as a result of the strain. The net excess energy of an electron is thus

$$\Delta E^p = \hbar\vec{v}\cdot(\Delta\vec{k} - \Delta\vec{k}_F). \tag{20}$$

The energy shift ΔE^G calculated by GG is defined in terms of an "unscaled" change of wave vector

$$\Delta\vec{k}_F^u = -\hat{v}(\Delta E^G - \Delta E_F)/\hbar v, \tag{21}$$

where $\Delta\vec{k}_F^u = \Delta\vec{k}_F + \underline{\epsilon}\cdot\vec{k}_F = \Delta\vec{k}_F - \Delta\vec{k}$. By combining Eqs. (20) and (21) we find that $\Delta E^p = \Delta E^G - \Delta E_F$, so the rate at which work is done on the electrons for the path integral in Eq. (1) becomes

$$\vec{\Pi}\cdot\vec{v} = iqu(\Delta E^G - \Delta E_F). \tag{22}$$

Note that ΔE_F vanishes for volume-conserving (shear) strains. Its value for hydrostatic strain is given in Ref. 16.

In order to make use of the energy shifts calculated by GG, an interpolation function must be found so that energy shifts at points other than those calculated can be approximated. The function must have the symmetry of the strained lattice. Using a procedure described elsewhere,[17] we obtained the interpolation functions for each of the basic strains as given in Table I.

Next, the ultrasonic strains employed in the experiments must be written as a linear combination of six basic strains $\underline{\epsilon}_j$, which we took to be the hydrostatic strain, the tetragonal extensions along [001] and [100], and the trigonal extensions along

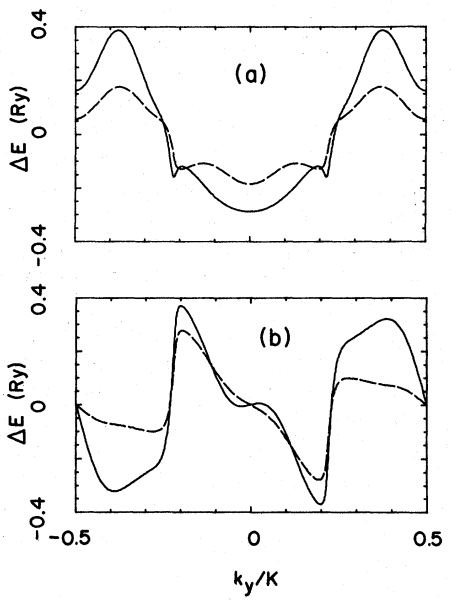

FIG. 3. Electron energy shift in Ry/(unit strain) for the central open orbit along [110]. The dashed curve is the interpolation function fitted to the points calculated by Gray and Gray in Ref. 12. The solid curve is the experimentally fit model deformation potantial. (a) Polarization along $\vec{B}$. (b) Polarization perpendicular to $\vec{B}$.

[111], [$\bar{1}$11], and [$\bar{1}\bar{1}$1], respectively. Thus we solve

$$\underline{\epsilon} = -\frac{\vec{q}\vec{u} + \vec{u}\vec{q}}{2\omega} = \frac{qu}{\omega} \sum_{j=1}^{6} c_j \underline{\epsilon}_j \tag{23}$$

for the c_j, and compute

$$\Delta E(\underline{\epsilon}, \vec{k}) = \sum_{j=1}^{6} c_j \Delta E^G(\underline{\epsilon}_j, \vec{k}) \tag{24}$$

for each ultrasonic strain. The nonzero c_j for $\vec{u} \parallel \vec{B}$ are $c_2 = 2/3\sqrt{2}$, $c_4 = 1/6\sqrt{2}$, and $c_5 = c_6 = 1/4\sqrt{2}$. For $\vec{u} \perp \vec{B}$, they are $c_2 = 2/3\sqrt{6}$, $c_3 = 4/3\sqrt{6}$, and $c_6 = -c_5 = 1/4\sqrt{6}$. Here and in Table I $\hat{k}_1$, $\hat{k}_2$, and $\hat{k}_3$ are along the crystal axes.

The energy shifts for the two ultrasonic strains used in the experiments are shown for the central orbit of the open-orbit band by the dashed lines in Fig. 3, plotted as functions of k_y. Note that $\Delta E(k_y)$ for $\vec{u} \parallel \vec{B}$ is symmetric, while $\Delta E(k_y)$ for $\vec{u} \perp \vec{B}$ is antisymmetric. One could have predicted these symmetries from the symmetries of the Fermi surface and of the respective strains. Consider again the coordinate system with x along $\vec{q}$, z along $\vec{B}$, and y along $\vec{B} \times \vec{q}$. The strain tensor $\underline{\epsilon}_{\parallel}$ for $\vec{u} \parallel \vec{B}$ vanishes except for $\epsilon_{xz} = \epsilon_{zx}$, whereas $\underline{\epsilon}_{\perp}$ for $\vec{u} \perp \vec{B}$ has only $\epsilon_{xy} = \epsilon_{yx}$ nonzero. These orbits have a reflection symmetry operation $\underline{\sigma}_y$ about the $k_y = 0$ plane. The strain tensor $\underline{\epsilon}_{\parallel}$ is even under a similarity transformation $\underline{\sigma}_y$, while $\underline{\epsilon}_{\perp}$ is odd. Since ΔE will have the symmetry of the strain, the results noted above follow.

The interpolation functions for ΔE are used in a numerical calculation of the Fourier coefficients defined in Eq. (4), with $\vec{\Pi} \cdot \vec{v}$ given by Eq. (22).[18] These coefficients are then substituted into Eq. (16) to find α_{def}, the deformation attenuation. Of course, one must also evaluate $\vec{E}^{sc} \cdot \vec{v}_n$ in order to make the calculation self-consistent. Furthermore, we have made no mention of the effects of those electrons not on the open-orbit bands.

Fortunately, some of the main features of the experimental data are reproduced by α_{def}, the attenuation calculated for the deformation force alone using Eq. (16). The solid curves in Fig. 4 show α_{def} for the two polarizations. Note the enhancement of the odd harmonics for $\underline{\epsilon}_{\parallel}$ and even for $\underline{\epsilon}_{\perp}$, in qualitative agreement with the experimental curves shown in Fig. 2. The harmonic structure is explainable by the shapes of the $\Delta E/v_x$ plots in Fig. 5. For $ql \gg 1$, α_{def} at $D/\lambda = n$ is proportional to $|a_n|^2$ averaged over k_z. If

$$\Delta E(k_y + \tfrac{1}{2}K)/v_x(k_y + \tfrac{1}{2}K) = \Delta E(k_y)/v_x(k_y),$$

only even harmonics will be present.[19] If

$$\Delta E(k_y + \tfrac{1}{2}K)/v_x(k_y + \tfrac{1}{2}K) = -\Delta E(k_y)/v_x(k_y),$$

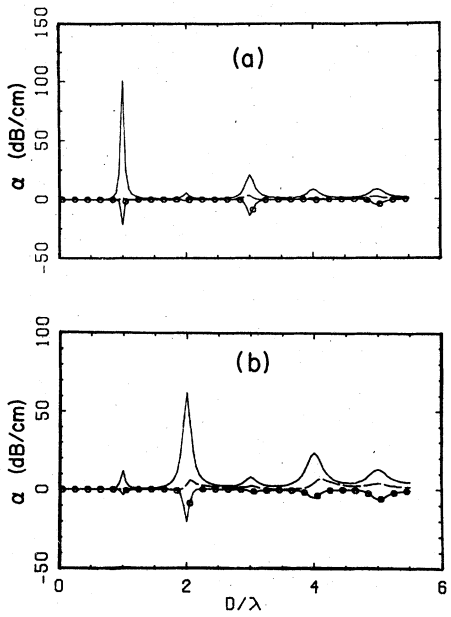

FIG. 4. Contributions of open-orbit electrons to the total attenuation for a deformation potential fitted to the calculations in Ref. 12. This deformation potential is also used in Figs. 5 and 8–11. The solid curves represent α_{def}, the dashed curves α_{sc}, and the circled α_i. (a) Polarization parallel to $\vec{B}$, $ql_x = 36$. (b) Polarization perpendicular to $\vec{B}$, $ql_x = 26$.

only odd harmonics will be present. Figure 5 shows that $\Delta E/v_x$ for $\underline{\epsilon}_{\parallel}$ approximately satisfies the first criterion, while for $\underline{\epsilon}_{\perp}$ the second is approximately satisfied. These symmetries are a

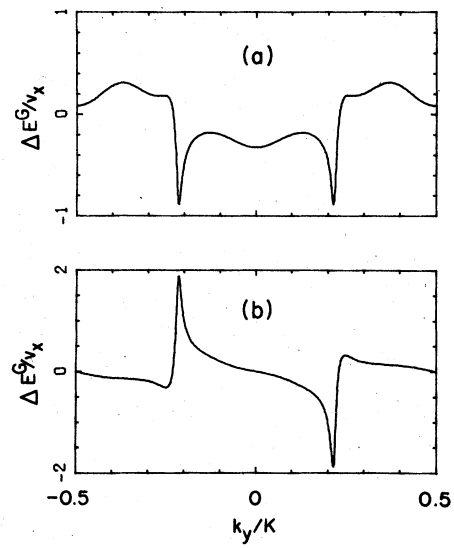

FIG. 5. $\Delta E^G/v_x$ along the central open orbit for (a) polarization parallel to $\vec{B}$, and (b) polarization perpendicular to $\vec{B}$. ΔE^G is in Ry/(unit strain), and v_x is in units of v_0, the free-electron Fermi velocity for copper.

consequence of the fact that the four bands of open orbits which lie in the four quadrants of the $k_x k_z$ plane are related through both inversion and translation by $\frac{1}{2}K$ along k_y.

Electrons from the remainder of the Fermi surface must be included and the calculation must be made self-consistent. These are on closed orbits for $0.15<|k_z a_0/2\pi|<0.87$, and open orbits along k_x for $|k_z a_0/2\pi|<0.15$.

In order to simplify the remaining calculations we assumed that these electrons were on a spherical free-electron Fermi surface with radius k_0 and relative density of states N. In the final calculations k_0 and N could be treated as adjustable parameters. The mean free path for these electrons was taken to be equal to l_x.

In order to find $\vec{E}^{sc}$ from Eq. (11) one must calculate $\underline{\sigma}$ for both open and closed orbits, invert it, and multiply it by the total deformation current. The conductivity for the spherical Fermi surface was calculated from the equations in Ref. 3. Because of the symmetries of the four bands of open orbits running along k_y, the integral in Eq. (9) can be reduced to an integration over a single band of open orbits in the expression

$$\underline{\sigma}=4\sigma_0\left(\frac{3}{16\pi}\right)^{1/3}\frac{Ka_0}{2\pi}\sum \mathrm{Re}\frac{\int \vec{v}_n^{\,*}\vec{v}_n\, d(k_z a_0/2\pi)}{1+iql_x(1-n\lambda/D)}, \qquad (25)$$

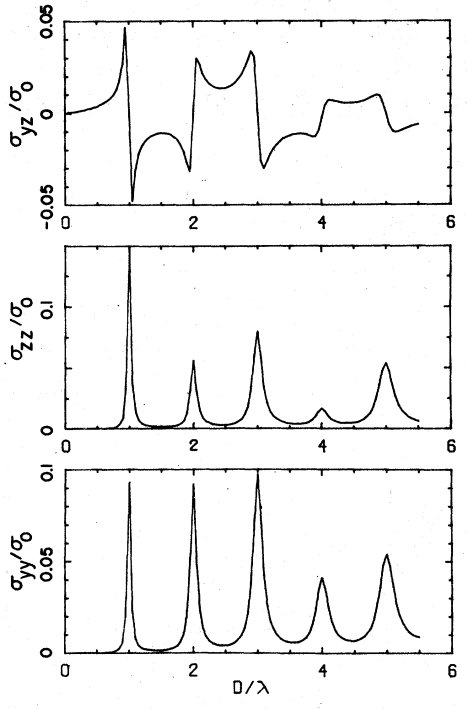

FIG. 6. Field-dependent elements of the conductivity tensor for copper resulting from open orbits when $\vec{B}$ is along $[11\bar{2}]$. Here $ql_x=36$ and $\sigma_0=ne^2\tau_0/m$, where $\tau_0=l_x/v_0$ and $v_0=\hbar(3\pi^2 n)^{1/3}/m$.

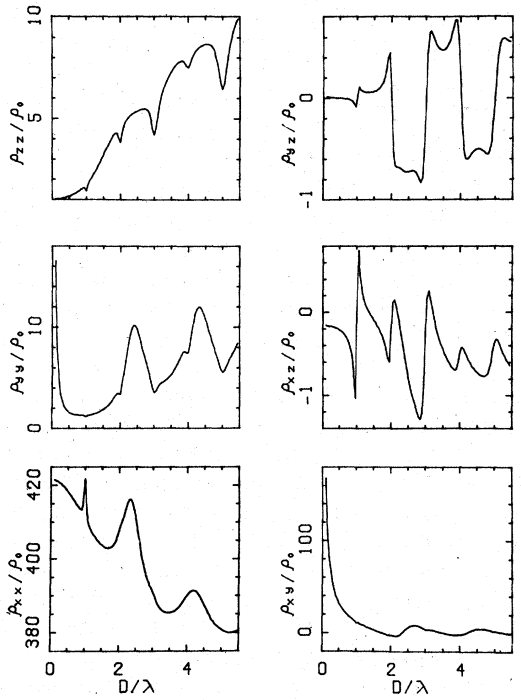

FIG. 7. Field-dependent elements of the resistivity tensor for the combination of the open-orbit conductivity in Fig. 6 and that for a free-electron spherical Fermi surface ($\rho_0=1/\sigma_0$).

where $\sigma_0=ne^2\tau_0/m$, $\tau_0=l_x/v_0$, $v_0=\hbar(3\pi^2 n)^{1/3}/m$, $n=4/a_0^3$, and a_0 is the length of the unit cell containing four conduction electrons. With the assumption that l_x is constant we find $\sigma_{xy}=\sigma_{yx}=0$. Furthermore,

$$\sigma_{xx}=4\sigma_0\left(\frac{3}{16\pi}\right)^{1/3}\frac{Ka_0}{2\pi}\frac{K_z a_0}{2\pi}(1+q^2l_x^2)^{-1}, \qquad (26)$$

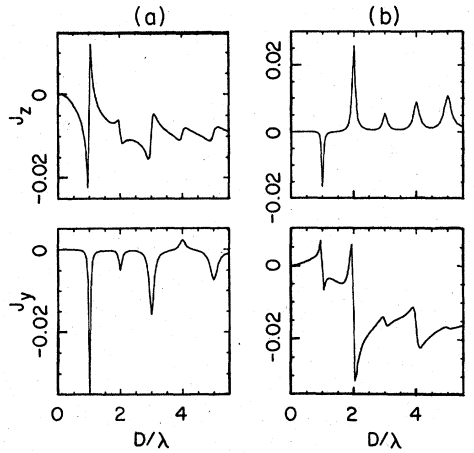

FIG. 8. Open-orbit contributions to the deformation current in units of neu for $ql=36$. (a) Polarization along $\vec{B}$. (b) Polarization perpendicular to $\vec{B}$.

$$\sigma_{xz}=\sigma_{zx}=4\sigma_0\left(\frac{3}{16\pi}\right)^{1/3}\frac{Ka_0}{2\pi}(1+q^2l_x^2)^{-1}\int\frac{\bar{v}_z}{\bar{v}_x}\,dk_z, \quad (27)$$

where K_z is the width of an open orbit band and $\bar{v}_i$ is the average of v_i on an orbit. The field-dependent elements of the open-orbit conductivity are shown in Fig. 6. The resistivity tensor elements obtained by inverting the total conductivity are shown in Fig. 7. Open orbit resonances cause peaks in ρ_{xx} and dips in ρ_{yy} and ρ_{zz}. This is consistent with Sievert's results[9] for overlapping cylindrical Fermi surfaces in the free-electron model.

The deformation currents caused by the open orbits are shown in Fig. 8. Note the large resonant current in the y direction for $\hat{u}\parallel\vec{B}$, and in the z direction for $\hat{u}\perp\vec{B}$. These arise because the Fermi surface does not have central symmetry in the planes containing the open orbits. The open-orbit currents are added to those from the free-electron sphere and multiplied by the total resistivity tensor to give the self-consistent electric field components shown in Fig. 9. These are substituted in Eqs. (17) and (18) to obtain α_{sc} and α_i, respectively.

The contributions of the open orbits to α_{def}, α_{sc}, and α_i are shown in Fig. 4 for the two polarizations. Closed-orbit contributions are shown in Fig. 10. The total self-consistent attenuations

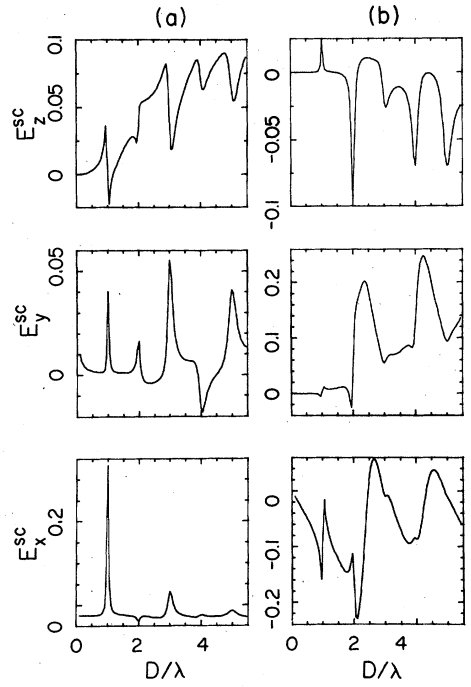

FIG. 9. Self-consistent electric field in units of neu/σ_0 for $ql_x=36$. (a) Polarization parallel to $\vec{B}$. (b) Polarization perpendicular to $\vec{B}$.

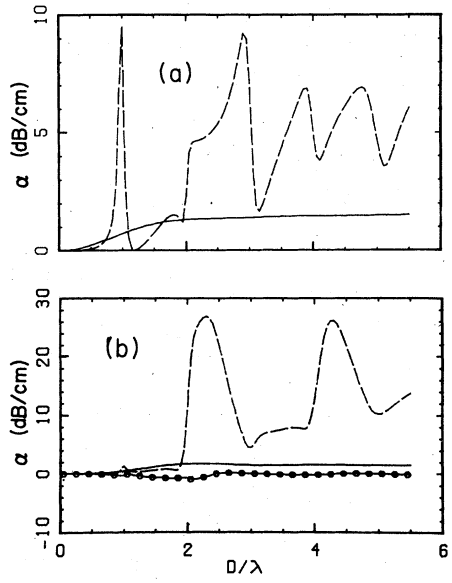

FIG. 10. Closed-orbit contributions to the total attenuation. The solid curves represent α_{def}, the dashed curves α_{sc}, and the circled α_i. (a) Polarization parallel to $\vec{B}$, $ql=36$. (b) Polarization perpendicular to $\vec{B}$, $ql=26$.

are shown in Fig. 11. It is obvious that the deformation contribution from the open orbits is the principal mechanism for the open-orbit resonances. For $\hat{u}\perp\vec{B}$ the self-consistent field term

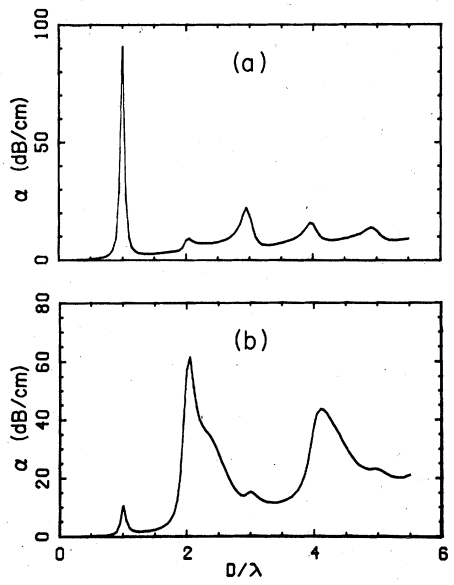

FIG. 11. Total self-consistent attenuation calculated for a deformation-potential function fitted to the energy shifts calculated for copper in Ref. 12. (a) Polarization parallel to $\vec{B}$, $ql=36$. (b) Polarization perpendicular to $\vec{B}$, $ql=26$.

TABLE II. Deformation-potential basis functions f_j and expansion coefficients b_j for ultrasonic strains. The b_j are given in Ry/(unit strain). The notation used here is that

$$C(\tfrac{1}{2}x+\tfrac{1}{2}y+z)\equiv\cos(\tfrac{1}{2}k_1a_0+\tfrac{1}{2}k_2a_0+k_3a_0)$$

for crystal coordinates, and

$$S(X-\tfrac{1}{2}Z)S(Y)\equiv\sin(k_q a_0/\sqrt{3}-\tfrac{1}{2}k_B a_0/\sqrt{6})\sin(k_p a_0/2\sqrt{2})$$

for experimental coordinates, where $\hat{P}=\hat{B}\times\hat{q}$.

	j	b_j	f_j (crystal coordinates)	f_j (experimental coordinates)
$\epsilon_{\parallel}$	1	0.0999	$C(\frac{1}{2}x+\frac{1}{2}z)+C(\frac{1}{2}y+\frac{1}{2}z)-2C(\frac{1}{2}x+\frac{1}{2}y)$	$-2C(X+Z)+2C(X-\frac{1}{2}Z)C(Y)$
	2	0.1256	$2C(z)-C(x)-C(y)$	$2C(X-2Z)-2C(X+Z)C(2Y)$
	3	0.0190	$C(\frac{1}{2}x-y-\frac{1}{2}z)+C(x-\frac{1}{2}y+\frac{1}{2}z)-2C(x+\frac{1}{2}y+\frac{1}{2}z)$	$4C(2X-Z)-[4C(2X+\frac{1}{2}Z)+10C(X+5Z/2)]C(Y)$
			$-2C(\frac{1}{2}x+y+\frac{1}{2}z)+4C(\frac{1}{2}x-\frac{1}{2}y+z)+4C(\frac{1}{2}x-\frac{1}{2}y-z)$	$+8C(X-2Z)C(2Y)+2C(X-\frac{1}{2}Z)C(3Y)$
			$+4C(\frac{1}{2}x+\frac{1}{2}y+z)-5C(\frac{1}{2}x-\frac{1}{2}z+y)-5C(x+\frac{1}{2}y-\frac{1}{2}z)$	
	4	0.1033	$C(x+z)+C(y+z)-2C(x+y)$	$-2C(2X+2Z)+2C(2X-Z)C(2Y)$
$\epsilon_{\perp}$	1	0.0989	$C(\frac{1}{2}x+\frac{1}{2}z)-C(\frac{1}{2}y+\frac{1}{2}z)$	$-2S(X-\frac{1}{2}Z)S(Y)$
	2	0.2018	$C(x)-C(y)$	$-2S(X+Z)S(2Y)$
	3	−0.0053	$C(x+\frac{1}{2}y-\frac{1}{2}z)-C(\frac{1}{2}x+y-\frac{1}{2}z)+2C(\frac{1}{2}x-\frac{1}{2}y+z)$	$-[4S(2X+\frac{1}{2}Z)+2S(X+5Z/2)]S(Y)$
			$-2C(\frac{1}{2}x-\frac{1}{2}y-z)+2C(x+\frac{1}{2}y+\frac{1}{2}z)-2C(\frac{1}{2}x+y+\frac{1}{2}z)$	$-4S(X-2Z)S(2Y)-6S(X-\frac{1}{2}Z)S(3Y)$
			$+3C(x-\frac{1}{2}y+\frac{1}{2}z)-3C(\frac{1}{2}x-y-\frac{1}{2}z)$	
	4	0.0441	$C(x+z)-C(y+z)$	$-2S(2X-Z)S(2Y)$

from the spherical Fermi surface in Fig. 10(a) shows magnetoacoustic oscillations which cause the bumps in Fig. 11(b) near $D/\lambda=2$ and $D/\lambda=4$. They are not seen in the experimental curve, indicating that representation of the closed orbits by a spherical Fermi surface is not valid in this respect.

V. EXPERIMENTALLY DETERMINED MODEL DEFORMATION POTENTIAL

Although the principal features of the experimental curves in Fig. 2 are reproduced by the calculated curves in Fig. 11, there is one obvious discrepancy: no dips appear in either of the calculated curves. We now consider whether some other deformation-potential function of the proper symmetry could yield smaller $\alpha_{\rm def}$ and $\alpha_{\rm sc}$, and larger negative α_i to cause dips.

Instead of using basis functions defined in terms of the basic crystal strains (hydrostatic, etc.) it becomes more convenient to pick basis functions which are natural to the ultrasonic strains $\epsilon_{\parallel}$ and $\epsilon_{\perp}$. A model deformation potential can then be expanded in terms of these basis functions and the coefficients varied until the sizes of the resonances are approximately the same as those found experimentally.

Using the method described in Ref. 17 we obtained four basis functions $f_j(\vec{k})$ for each of the experimental strains as shown in Table II, thus we can write

$$\Delta E(\vec{k})=\sum_{j=1}^{4} b_j f_j(\vec{k}). \tag{28}$$

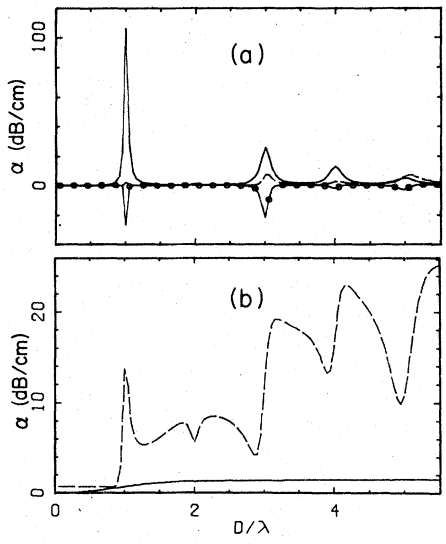

FIG. 12. Contributions to the attenuation when polarization is parallel to $\vec{B}$ for a deformation potential fitted to experimental data. This deformation potential is also used in Figs. 13 and 14. The solid curves represent $\alpha_{\rm def}$, the dashed curves $\alpha_{\rm sc}$, and the circled α_i. (a) Open-orbit contributions. (b) Closed-orbit contributions.

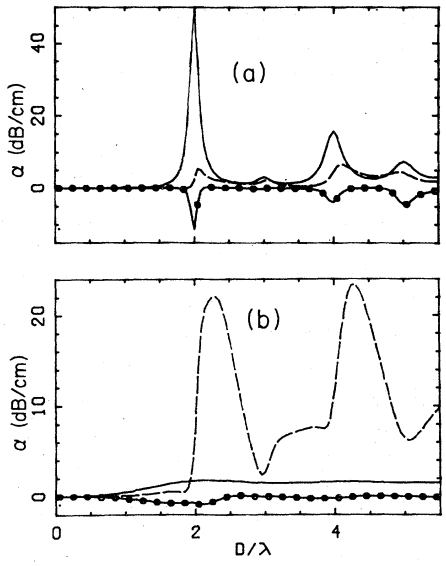

FIG. 13. Contributions to the attenuation for polarization perpendicular to $\vec{B}$. (a) Open-orbit contributions. (b) Closed-orbit contributions.

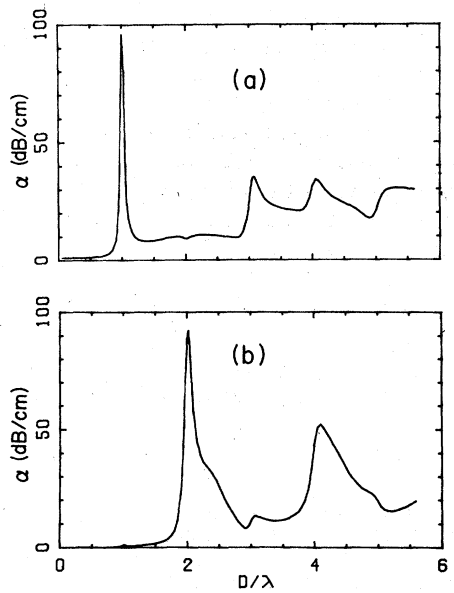

FIG. 14. Total self-consistent attenuation calculated with a deformation potential fitted to experimental data. (a) Polarization parallel to $\vec{B}$. (b) Polarization perpendicular to $\vec{B}$.

This expansion, combined with Eqs. (4) and (22), leads to

$$a_n = \frac{i\omega}{K} \sum b_j \int_{-K/2}^{K/2} \frac{f_j}{v_x} \exp\left(\frac{2\pi i n k_y}{K}\right) dk_y . \qquad (29)$$

In an attempt to produce dips in the attenuation the b_j were chosen so that $\alpha_{\text{def}}(n=2)=0$ for $\epsilon_{\parallel}$ and $\alpha_{\text{def}}(n=1)=0$ for $\epsilon_{\perp}$. In addition the larger peaks were made to have magnitudes near those measured. The resulting coefficients for the model deformation potential are given in Table II.

The various contributions to the attenuation for this model are shown in Figs. 12 and 13 for the two strains. In Fig. 12(b) we see that α_{sc} for the closed orbits has a small dip at $n=2$ which leads to a very slight dip in the total attenuation shown in Fig. 14(a). There can be no dip at $n=1$ for $\epsilon_{\perp}$ because there is essentially no background attenuation which could have a dip. Thus, unless one can find a mechanism for the high-field attenuation found experimentally, there is no hope of obtaining a dip in the model calculation. The frequency dependence of the depth of the dip indicates that the background attenuation increases linearly with frequency.

The model deformation potential is compared with the interpolation function based on the calculations of GG in Fig. 3. The two sets of functions coincide in the vicinity of the Q and P points calculated by GG on the necks of the Fermi surface. The overall agreement is surprisingly good, considering that there were no adjustable parameters in the calculation using the interpolation function.

VI. SUMMARY AND CONCLUSIONS

Our experiments have confirmed the existence of dips as well as peaks in the open-orbit resonant attenuation for $\vec{q} \| [111]$ and $\vec{B} \| [1\bar{2}1]$. A model calculation using Pippard's theory and a deformation potential consisting of an interpolation function fitted to energy-band shifts calculated by Gray and Gray agree well with the experimental results except that it fails to give any dips.

A parametrized model deformation potential leads to a small dip for the $n=2$ resonance with $\vec{u} \| \vec{B}$, but cannot give a dip for the $n=1$ resonance with $\vec{u} \perp \vec{B}$ because the calculated background attenuation vanishes in the high-field limit for our model. Possible explanations for this failure are listed below.

Free-electron approximation for all but the resonant open orbits. This approximation greatly reduced the computational effort but is the most likely cause of the failure to get a high-field dip. The next simpler approximation which might improve the calculation would be to introduce a simple additional deformation potential over the spherical Fermi surface to increase the deformation current while retaining the same conductivity.

Constant ql_x. The effect of assuming ql_x to be constant on the open orbits causes σ_{xy} to vanish for these orbits. However, the closed orbits dominate the conductivity anyway, so this approximation is probably not important.

Perfect screening. The assumption that the total current is zero implies perfect screening. The correct treatment would simply replace Eq. (11) by Maxwell's equations. For free electrons Mertsching[20] shows that this causes the high-field attenuation to approach $\omega^2\tau^2/(1+4ql/3\pi)$ times the zero-field value. At the frequencies employed here this amounts to a correction of only a few percent, insufficient to explain the high-field discrepancies.

We have shown the feasibility of determining the strain dependence of the Fermi surface of a metal which supports open orbits by fitting open-orbit resonance data to a parametrized model calculation. It should be possible to determine the deformation potential over most of the Fermi surface by using a variety of orientations of $\vec{B}$ and $\vec{q}$.

ACKNOWLEDGMENTS

We wish to thank C. M. Casteel for his assistance in carrying out the experiments and the calculations, Brian Mulvaney for his help in finding the interpolation functions, and P. R. Antoniewicz and L. Kleinman for helpful discussions of the theory. This work was supported by National Science Foundation Grant No. DMR 76-11331.

---

*Present address: Air Force Avionics Laboratory, Wright-Patterson AFB, Ohio 45433.

[1]S. Rodriguez, Phys. Rev. 112, 80 (1958).
[2]T. Kjeldaas, Jr., Phys. Rev. 113, 1473 (1959).
[3]M. H. Cohen, M. J. Harrison, and W. A. Harrison, Phys. Rev. 117, 937 (1960).
[4]A. B. Pippard, Proc. R. Soc. A 257, 165 (1960).
[5]See, for example, V. L. Gurevich, Soc. Phys. JETP 10, 51 (1960) [Zh. Eksp. Teor. Fiz. 37, 71 (1959)].
[6]J. R. Boyd and J. D. Gavenda, Phys. Rev. 152, 645 (1966).
[7]S. G. Eckstein, Phys. Rev. Lett. 16, 611 (1966).
[8]C. W. Burmeister, D. B. Doan, and J. D. Gavenda, Phys. Lett. 7, 112 (1963).
[9]Paul R. Sievert, Phys. Rev. 161, 637 (1967).
[10]E. A. Kaner, V. G. Peschanskii, and I. A. Privorotskii, Sov. Phys. JETP 13, 147 (1961) [Zh. Eksp. Teor. Fiz. 40, 214 (1961)].
[11]D. S. Khatri and J. R. Peverley, Phys. Rev. Lett. 30, 490 (1973).
[12]D. M. Gray and A. M. Gray, Phys. Rev. B 14, 669 (1976).
[13]Obtained from A. F. Clark, Natl. Bur. Stand. (U.S.), Boulder, Colo.
[14]Further experimental details can be found in W. M. Theis, Ph.D. thesis (University of Texas at Austin, 1977) (unpublished).
[15]S. J. Chang and J. D. Gavenda, Phys. Rev. B 9, 1240 (1974).
[16]H. L. Davis, J. S. Faulkner, and H. W. Joy, Phys. Rev. 167, 601 (1968).
[17]W. M. Theis, Brian Mulvaney, and J. D. Gavenda (unpublished).
[18]Electron velocities were computed from the functions fitted by M. R. Halse, Phil. Trans. R. Soc. 265, 507 (1969).
[19]Philip Franklin, *Fourier Methods* (McGraw-Hill, New York, 1949).
[20]J. Mertsching, Phys. Status Solidi 37, 465 (1970).